

# Optical Properties of Human Trabecular Meshwork in the Visible and Near-Infrared Region

Stuart K. Farrar, MS,<sup>1</sup> Cynthia Roberts, PhD,<sup>1,2\*</sup> William M. Johnston, PhD,<sup>3</sup>  
and Paul A. Weber, MD<sup>2</sup>

<sup>1</sup>Biomedical Engineering Center, Ohio State University, Columbus, Ohio 43210

<sup>2</sup>Department of Ophthalmology, College of Medicine, Ohio State University, University  
Hospitals Clinic, Columbus, Ohio 43210

<sup>3</sup>College of Dentistry, Ohio State University, Columbus, Ohio 43210

**Background and Objectives:** Despite disparate treatment parameters, similar success in laser trabeculoplasty (LT) is attained using the argon (514.5 nm) and diode (810 nm) laser. However, the mechanism of this success remains unresolved. To further understand LT, this study characterizes the optical properties of trabecular meshwork (TM).

**Study Design/Materials and Methods:** Reflectance was measured from 10 TM samples over wavelengths of 400–820 nm, using an integrating sphere/spectrophotometer. Corrections were made for reflections at boundaries of refractive index mismatch. Kubelka-Munk coefficients were calculated and converted to linear transport coefficients.

**Results:** Scattering greatly dominated absorption. The scattering and absorption coefficients were, respectively,  $141.20 \pm 15.80 \text{ cm}^{-1}$  and  $4.89 \pm 1.95 \text{ cm}^{-1}$  at 514.5 nm, and  $94.44 \pm 15.03 \text{ cm}^{-1}$  and  $0.0874 \pm 0.111 \text{ cm}^{-1}$  at 810 nm (estimated anisotropy of 0.90). The corresponding penetration depths ( $1/e$ ) were 69  $\mu\text{m}$  (514.5 nm) and 106  $\mu\text{m}$  (810 nm).

**Conclusion:** The absorption coefficient of 514 nm energy is two orders of magnitude greater than 810 nm energy, while scattering coefficients are much closer. The fluence used at 514.5 nm is higher at the surface than that at 810 nm, but falls below it deep within the TM due to the differential absorption. Therefore, similar initial therapeutic effects are obtained with 810 nm using less total absorbed energy. Thermal damage resultant from excess energy deposited at 514.5 nm may be related to the lack of success in repeat argon LT, pointing out the need for studies of repeat diode LT. *Lasers Surg. Med.* 25:348–362, 1999.

© 1999 Wiley-Liss, Inc.

**Key words:** laser trabeculoplasty; integrating sphere; Kubelka-Munk theory; absorption and scattering coefficients; anisotropy

## INTRODUCTION

The main modes of therapy for primary open angle glaucoma (POAG) are through pharmaceuticals, laser trabeculoplasty, and other surgical interventions. Laser trabeculoplasty (LT) is successfully used in treating early POAG, by increasing the outflow of aqueous humor. The more popular of the two current clinical treatment regimes for LT uses an argon laser at 514.5 nm, while the

Contract grant sponsor: Ohio Lions Eye Research Foundation; Contract grant sponsor: Central Ohio Lions Eyebank; Contract grant sponsor: Department of Ophthalmology, Ohio State University.

\*Correspondence to: Cynthia Roberts, Ph.D., Biomedical Engineering Center, Ohio State University, 270 Bevis Hall, 1080 Carmack Road, Columbus, OH 43210.

E-mail: Roberts.8@osu.edu

Accepted 4 June 1999

other uses a diode laser at 810 nm. The trabecular meshwork (TM) is usually irradiated at 25 evenly spaced points per quadrant, for a total of 50 points across 180° or 100 points about the circumference of the TM. For both lasers, the end point of each exposure is a transient blanching of the TM and, in the case of the argon laser, a possible formation of a small bubble [1,2]. Since the near-infrared light is typically less absorbed by pigmented tissue than visible wavelengths, the power settings for the diode laser must be higher than the argon laser settings to produce the desired blanching, given the clinical laser parameters in use. The typical power settings for the argon laser are from 500–1,200 mW with an average of approximately 800 mW, with a spot size of 50  $\mu$ m and a 0.1-sec duration [3–7]. It is the practice of some surgeons to use a single fixed power setting on every patient, regardless of the blanching [2]. In contrast, the typical diode laser power settings are 700–1,500 mW with an approximate average of 1,100 mW, a spot size of 100  $\mu$ m, and a 0.2-sec duration [1,4,5,8–10]. Argon laser trabeculoplasty, as a means of controlling intraocular pressure (IOP), has an approximate 50% failure within 5 years [11–17] and as high as 50% failure in 2 years [3]. Diode LT has similar clinical results, but there have been few long-term studies. Studies include 2-year follow-ups [1,4,9] and a 5-year follow-up [18]. The similar clinical results, despite the differences in treatment parameters, raise questions as to the mechanism of action.

There is no consensus on the mechanism of LT. Initially introduced by Wise and Witter [19] in 1979, it was believed that the mechanism was mechanical, and that thermal damage to collagen fibrils at the points of treatment caused contraction, and a corresponding reduction in circumference of the TM ring. This in turn would cause an increase in the size of the intertrabecular spaces, expansion of a collapsed canal of Schlemm, and enhanced outflow and lower IOP [20–22]. Another mechanical theory proposed that the increase in intertrabecular spaces was due to degeneration of trabeculae upon treatment [23]. A more recent theory suggests that a biological mechanism is responsible for the reduction in IOP, with the laser energy causing upregulation in TM endothelium cells surrounding the treatment sites. These trabeculae can then better perform the task of extracellular matrix turnover, clearing debris from the trabecular space [24–26].

In an effort to increase understanding of the similar initial clinical results despite differences

in treatment parameters, the goal of this study was to measure the TM optical properties from 400–820 nm and determine the absorbed energy distribution within the TM at the prevalent wavelengths used clinically in laser trabeculoplasty. This may have implications for how this procedure is optimized.

## MATERIALS AND METHODS

### Sample Collection

Human trabecular meshwork was collected from 80 eyes obtained from the Central Ohio Lions Eye Bank at The Ohio State University. Each globe was transected along a frontal plane approximately 3–5 mm posterior to the limbus. The anterior chamber, including the iris and ciliary body, was then bisected. Under a dissecting microscope (5 $\times$ ), the iris and ciliary body were pulled away from the scleral spur. Increasing magnification to 25 $\times$ , the ring of trabecular meshwork was gently coaxed out of the scleral sulcus with forceps and a scalpel. Care was taken to exclude Descemet's membrane, the scleral spur, and remnants of the iris. The strands of TM from each pair of eyes were stored separately in buffered saline at 4°C until there was sufficient quantity of tissue to perform spectral analysis.

The 80 specimens of TM were divided into 10 unique samples, each consisting of TM from four pairs of eyes. Each sample was then homogenized (PowerGen 125 with a 7-mm sawtooth probe, Fisher Scientific, Pittsburgh, PA), and then centrifuged at approximately 500g for 10 minutes. Excess saline was pipetted from the samples that were then mixed to ensure homogeneity.

### Spectrophotometry and Data Measurements

Reflectance data were obtained using a double-beam, UV-VIS Spectrophotometer and integrating sphere (Model Lambda 6, Perkin Elmer, Oak Brook, IL). In this system, two collimated parallel beams of light are alternately projected into the sphere, which has a diffuse reflective interior coating of barium sulfate. These beams alternate, one serving as a reference while the other strikes the tissue sample at the back of the sphere. A photodetector mounted perpendicular to the beams measures the intensity of the diffuse reflected light from each beam in turn. The reflectance, which is the relative intensity of the reflected target beam to the reference beam, is re-

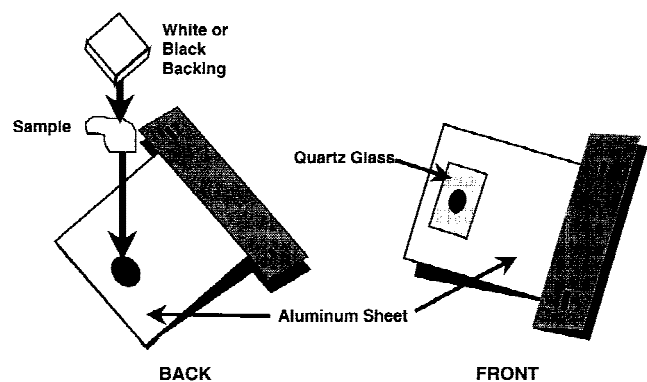


Fig. 1. The aluminum holder, with quartz glass front and opaque black or white backing, conformed the samples to an average thickness of  $610 \pm 10 \mu\text{m}$ . The aluminum front was painted flat white, matching the interior of the integrating sphere.

corded for wavelengths of 400–820 nm at steps of 1 nm.

Before measuring the reflectance of samples, a background correction was performed with a standardized white porcelain tile [27]. A calibration process followed, in which two relative reflectance spectra of a white tile standard, whose absolute reflectance is traceable to National Institute of Standards and Technology (NIST) Standard Reference Material, were measured and averaged. Two additional sets were also measured and averaged with a black tile standard. Finally, the reflectance was measured six times for each sample, three times with a black backing behind the sample, and three times with a white backing behind the sample. Each of the above sets of spectra was averaged to improve the signal to noise ratio. The relative reflectance data of the sample were then converted to absolute reflectance by interpolation at every wavelength.

### Holder Design and Sample Thickness

A sample holder was designed to conform the amorphous samples to a desired thickness, and to fit the existing spectrophotometer holder (Fig. 1). The sample needed to be thin enough that light from the target beam reached the backing behind the sample, producing differences between reflectance values using the white and black backings. However, the sample needed to be thick enough to produce measurable effects on the beam.

Tissue holders were made from aluminum sheets of different thicknesses. These sheets were cut and molded to fit over the standard spectrophotometer holder at the back of the integrating sphere. A 5-mm hole was drilled in each sheet,

such that the target beam was aligned with the center of the hole. The surface of the aluminum exposed to the beam was painted to match the interior surface of the sphere. A  $12 \times 9 \text{ mm}$  piece of quartz glass was glued over the hole onto the painted surface of the aluminum. Quartz was chosen because it attenuates the beam less than glass for the wavelengths of interest. The tissue well was formed by the quartz glass and the edges of the hole. The sample was then placed into the well and covered with either a black or white backing. The final holder conformed the tissue to an average sample thickness of  $610 \pm 10 \mu\text{m}$ , based on repeated measurements with a micrometer.

### Interface Reflections

During the background correction and referencing process, glycerol was placed in the holder to serve as an index matching medium. Even with glycerol, the reflectance data had to be corrected for certain interface reflections. In this study, three classifications of reflections were considered to occur at a boundary mismatch. The first was when spectral or near-collimated light was incident normal to the boundary. The Fresnel reflection coefficient [28],  $r_F$ , gives the fraction of collimated light that is reflected.

The second type of reflection occurred when the light incident on the boundary was diffuse, and the light was traveling from a lower to higher index of refraction. While spectral light approaches a boundary at a defined angle, ideal diffuse light approaches from all angles. Walsh [29] calculated the total fraction of diffuse light reflected in this event,  $r_W$ , by integrating the general form of the Fresnel formula over the range of possible angles of incidence,  $0$ – $90^\circ$ . This yields

$$r_W = \frac{1}{2} + \frac{(n-1)(3n+1)}{6(n+1)^2} + \left[ \frac{n^2(n^2-1)^2}{(n^2+1)^3} \right] \ln \frac{(n-1)}{(n+1)} - 2n^3 \frac{(n^2+2n-1)}{(n^2+1)(n^4-1)} + \left[ \frac{8n^4(n^4+1)}{(n^2+1)(n^4-1)^2} \right] \ln n. \quad (\text{Eq. 1})$$

Finally, when diffuse light travels from a higher to lower index of refraction, the critical angle,  $\theta_C = \sin^{-1}(1/n)$ , must be taken into account before integrating the Fresnel formula. Light incident on the boundary at angles greater than  $\theta_C$  experience total internal reflection, while the reflection of light at incident angles less than  $\theta_C$  is

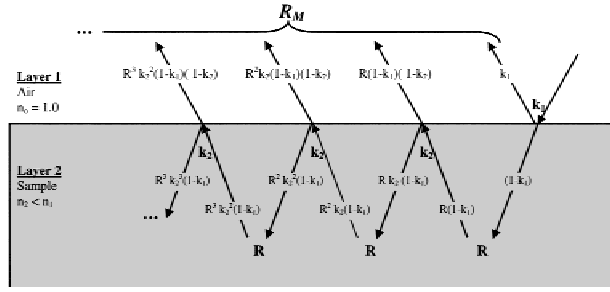


Fig. 2. A single boundary of refractive index mismatch, and the related interface reflections and transmissions, as explained in the Appendix, Section I. Layer 1 (air) is nonattenuating, and layer 2 is an absorbing and diffusely scattering medium. The value  $k_1$  is a spectral reflection coefficient, and  $k_2$  is a diffuse reflection coefficient (see Appendix, Section I). The desired value is the reflectance of the sample,  $R$ , which must be extracted from the measured reflectance,  $R_M$ . Reflection coefficients: air/quartz,  $k_1 = 0.04$  (Fresnel); quartz/air,  $k_2 = 0.5963$  (Richmond).

represented by the general form of the Fresnel formula. Richmond [28] accounted for the critical angle and derived the reflection coefficient,  $r_R$ ,

$$r_R = 1 - \frac{1 - r_W}{n^2}, \quad (\text{Eq. 2})$$

where  $r_W$  is the reflection coefficient derived by Walsh. The Richmond reflection coefficient is much greater than the Walsh coefficient, due to total internal reflection.

Corrections were made at three boundaries in this study, at which the above reflections occur. The first happens during the referencing process when glycerol is in the holder. In this case, the value desired after correcting for interface reflections is the reflectance that would be measured from the backing,  $R_g$ , if there were no mismatch of refractive indices. The boundary of mismatched indices of refraction is between the quartz glass, with a refractive index of 1.5, and the air within the integrating spheres (Fig. 2). The boundaries between quartz glass, glycerol, and backing have negligible differences in indices. Saunderson [30] derived an analytical relationship between  $R_g$  and  $R_m$ , using an identity for an infinite sum (see Appendix, Section I).

$$R_g = \frac{R_m - k_1}{1 + k_2 R_m - k_1 - k_2}. \quad (\text{Eq. 3})$$

As a Fresnel reflection coefficient, the value of the spectral reflection coefficient,  $k_1$ , between air and

quartz glass is 0.0400. From Equation 2 the value of the diffuse reflection coefficient,  $k_2$ , between the quartz glass and air is 0.5963.

The other two mismatched boundaries occur when measuring reflectance from the sample. As in the referencing process, interface reflections occur at the boundary between the air in the integrating sphere and the quartz glass. The other boundary is between the glass and the tissue (Fig. 3). While the glass has an index of refraction of 1.5, the TM is assumed to have index of approximately 1.37. This index is based on refractive indices of scleral collagen fibrils ( $n = 1.47$ ) and the surrounding matrix ( $n = 1.345$ ) [31–34], the refractive index of the cornea ( $n = 1.376$ ) [35], and the refractive index of the saline in which the TM was stored ( $n = 1.34$ ).

The light interacting between these two boundaries complicates the relationship between the measured reflectance  $R_M$ , and the desired reflectance  $R$  (see Appendix, Section II). The analytical relationship between the two is

$$R_M = k_1 + \frac{k_3(1 - k_1)^2}{1 - k_1 k_3} + \frac{R(1 - k_1)(1 - k_3)(1 - k_4)(1 - k_2)}{(1 - k_1 k_3)(1 - R k_4)(1 - k_2 k_5)} \cdot \left[ 1 - \frac{k_2 R(1 - k_4)(1 - k_5)}{(1 - R k_4)(1 - k_2 k_5)} \right]. \quad (\text{Eq. 4})$$

The variables  $k_1$  and  $k_2$  were given previously. As a Fresnel reflection coefficient, the value of the spectral reflection coefficient,  $k_3$ , between quartz glass and TM is 0.00205. From Equation 1 the value of the diffuse reflection coefficient,  $k_4$ , between TM and quartz glass is 0.0241. From Equation 2 the value of the diffuse reflection coefficient,  $k_5$ , between the quartz glass and TM is 0.1859. The index mismatch between the tissue sample and the backing was not accounted for, since there was not a straightforward technique for quantifying the interface reflections, due to the attenuating properties of the tissue.

### Kubelka-Munk Theory

Once the corrections were made to the reflectance data, Kubelka-Munk (KM) theory [36] was used to convert the measured reflectance data to KM scattering (S) and absorption coefficients (K). The KM theory describes a one-dimensional, two-flux mathematical model of the propagation of diffuse light. The incremental change in these



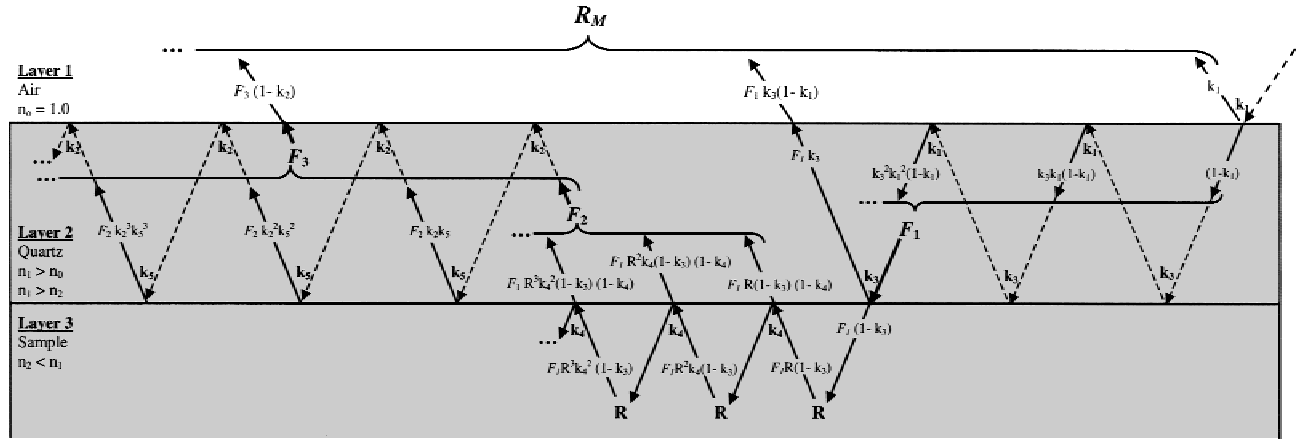


Fig. 3. Two boundaries of refractive index mismatch, and the related interface reflections and transmissions, as explained in the Appendix, Section II. Layers 1 and 2 are nonattenuating mediums, and layer 3 is an absorbing and diffusely scattering medium. The values  $k_1$  and  $k_3$  are spectral reflection coefficients, and  $k_2$ ,  $k_3$ , and  $k_4$  are diffuse reflection coefficients (see Appendix, Section II). The values  $F_1$ ,  $F_2$ , and  $F_3$  represent summations of propagating light. The desired value is the reflectance of the sample,  $R$ , which must be extracted from the measured reflectance,  $R_M$ . Reflection coefficients: air/quartz,  $k_1 = 0.04$  (Fresnel); quartz/air,  $k_2 = 0.5963$  (Richmond); quartz/sample,  $k_3 = 0.00205$  (Fresnel); sample/quartz,  $k_4 = 0.0241$  (Walsh); and quartz/sample,  $k_5 = 0.1859$  (Richmond)

fluxes, as a function of depth, can be written in the form of two differential equations [36]:

$$-\frac{di}{dx} = -(K + S)i + Sj, \quad \text{and} \quad \frac{dj}{dx} = -(K + S)j + Si. \quad (\text{Eq. 5 \& 6})$$

The diffuse flux  $i$ , entering the tissue in the negative direction, is either absorbed or scattered as  $x$  decreases from  $x = X$  to  $x = 0$ . The scattered part of  $i$  is only scattered in the positive direction, contributing to flux  $j$ . Flux  $j$  is also absorbed and scattered corresponding to  $K$  and  $S$ , with the scattered part of  $j$  contributing to  $i$ .

If a backing with reflectance  $R_g$  is placed behind the sample, the boundary conditions are  $i = I_0$  at  $x = X$ , and  $j = i R_g$  at  $x = 0$ , and Equations 6 and 7 can be integrated to yield the reflectance [36]

$$R = \frac{j(X)}{I_0} = \frac{1 - R_g(a - b \operatorname{ctgh}(bSX))}{a + b \operatorname{ctgh}(bSX) - R_g}, \quad (\text{Eq. 7})$$

$$\text{where } a = \frac{(S + K)}{S}, \quad b = \sqrt{a^2 - 1},$$

and  $\operatorname{ctgh}$  represents the hyperbolic cotangent function.

Two sets of reflectance data are obtained for each sample, one with a white backing,  $R_1$ , and one with a black backing,  $R_2$ . As stated previ-

ously, the reflectance of the two backings alone is known. They will be represented by  $R_{g1}$  for the white backing and  $R_{g2}$  for the black backing. In addition, the sample thickness,  $X$ , is set by the known depth of the sample holder. With these two sets of data and Equation 7, the values of  $S$  and  $K$  can be determined from 400–820 nm.

The spectrophotometer used in the study is optimized for the ultraviolet and visible range of wavelengths. At wavelengths in the near-infrared (IR) region, the noise in the signal increases, as the KM absorption coefficient falls steadily towards zero. To filter deviations that occurred occasionally above 800 nm due to noise, the definition of  $b$  in equation 7 was modified to take the square root of the absolute value of  $(a^2 - 1)$ .

Once the reflectance data were corrected for interface reflections and converted to KM coefficients, the coefficients were then transformed to linear transport absorption ( $\mu_a$ ) and scattering ( $\mu_s$ ) transport coefficients.

### Converting Linear Transport Coefficients

Although KM scattering coefficients describe the optical properties of a material, the more common representation of optical properties is the linear transport coefficients,  $\mu_a$  and  $\mu_s$ . Therefore, the theory of van Gemert and Star [37], valid for an anisotropically scattering medium, was used to find  $\mu_a$  and  $\mu'_s$ . The value  $\mu'_s$  is the reduced scattering coefficient equal to

$$\mu'_s = \mu_s (1 - g), \quad (\text{Eq. 8})$$

TABLE 1. Optical Properties of Collagenous Tissues [33, 38, 39]

Tissue type	Wavelength (nm)	$\mu_a$ (cm <sup>-1</sup> )	$\mu_s$ (cm <sup>-1</sup> )	Anisotropy
Human aorta	633	0.52	316	0.87
	1,064	0.5	239	0.90
Intima	476	0.81	237	0.81
	580	0.81	183	0.81
	600	0.81	178	0.81
	633	0.85	171	0.85
Media	476	0.89	410	0.89
	580	0.9	331	0.90
	600	0.89	323	0.89
	633	0.9	310	0.90
Adventitia	476	0.74	267	0.74
	580	0.77	217	0.77
	600	0.78	211	0.78
	633	0.81	195	0.81
Human dermis	633	2.7	187	0.81
Porcine sclera	1,064	~0.03	~44	0.9

where  $g$  is anisotropy of the material, calculated as the mean cosine of the scattering angle. Once obtained, the reduced scattering coefficient was converted to the scattering coefficient based on typical values of anisotropy in tissue. From the literature, Cheong et al. [38] and Cheong [39] nicely compiled optical properties of various tissues. Some of these data for collagenous tissues are listed in Table 1. In the last row of this table are properties for porcine sclera, reported by Hammer et al. [33].

Tissue tends to be extremely forward-scattering. To account for a possible range of anisotropy in TM based on the above data, two sets of  $\mu_s$  were calculated from the reduced scattering coefficient,  $\mu'_s$ , using estimated anisotropies of 0.85 and 0.90.

## RESULTS

From the measured reflectance values, the KM scattering and absorption coefficients were obtained (Fig. 4). These were then converted into linear transport coefficients (Fig. 5). For wavelengths of 400–820 nm, the scattering coefficient,  $\mu_s$ , greatly dominated the absorption coefficient,  $\mu_a$ . The values of  $\mu_a$  ranged from  $9.62 \pm 1.17$  cm<sup>-1</sup> at 400 nm to  $0.081 \pm 0.034$  cm<sup>-1</sup> at 820 nm. For  $g = 0.85$ , the values of  $\mu_s$  ranged from  $144.13 \pm 7.73$  cm<sup>-1</sup> at 400 nm to  $62.62 \pm 3.18$  cm<sup>-1</sup> at 820 nm. For  $g = 0.90$ , the values of  $\mu_s$  ranged from  $216.20 \pm 11.60$  cm<sup>-1</sup> at 400 nm to  $93.93 \pm 4.77$  cm<sup>-1</sup> at 820 nm.

Examining the wavelengths used clinically for laser trabeculoplasty, the values of the absorp-

tion, scattering, and attenuation coefficients are listed in Table 2. Based on an exponential attenuation, the penetration depths of the argon and diode laser, occurring when the energy within the tissue was diminished to 37% (1/e) or 13% (1/e<sup>2</sup>) of the initial setting, are also given in Table 2.

## DISCUSSION

The depth of the TM at the point of treatment is approximately 90–130  $\mu$ m, as estimated by average values of individual TM sheet thickness, number of sheets, intratrabecular space thickness (space between sheets), location of treatment, and juxtacanalicular thickness [40–42]. This range is in agreement with the findings of Dr. Douglas Johnston of the Mayo Clinic (personal correspondence) and Dr. Mark Johnson of MIT (personal correspondence). This thickness could vary among surgeons, depending on the anterior to posterior positioning of the laser beam on the TM.

Based on the 1/e penetration depth, 63% of the argon laser energy is deposited in the TM surface. Using the attenuation coefficients at the argon and diode laser wavelengths, and assuming an exponential decay of laser energy with increasing TM depth, the relative energy profile was plotted (Fig. 6). With typical parameters of LT given in the Introduction (800 mW for the argon laser and 1,100 mW for the diode laser), the values of total energy deposited on the TM surface would be approximately 80 mJ for the argon laser and 220 mJ for the diode laser. The different spot sizes of these regimes equate to a diode exposure area

## Kubelka-Munk Optical Coefficients

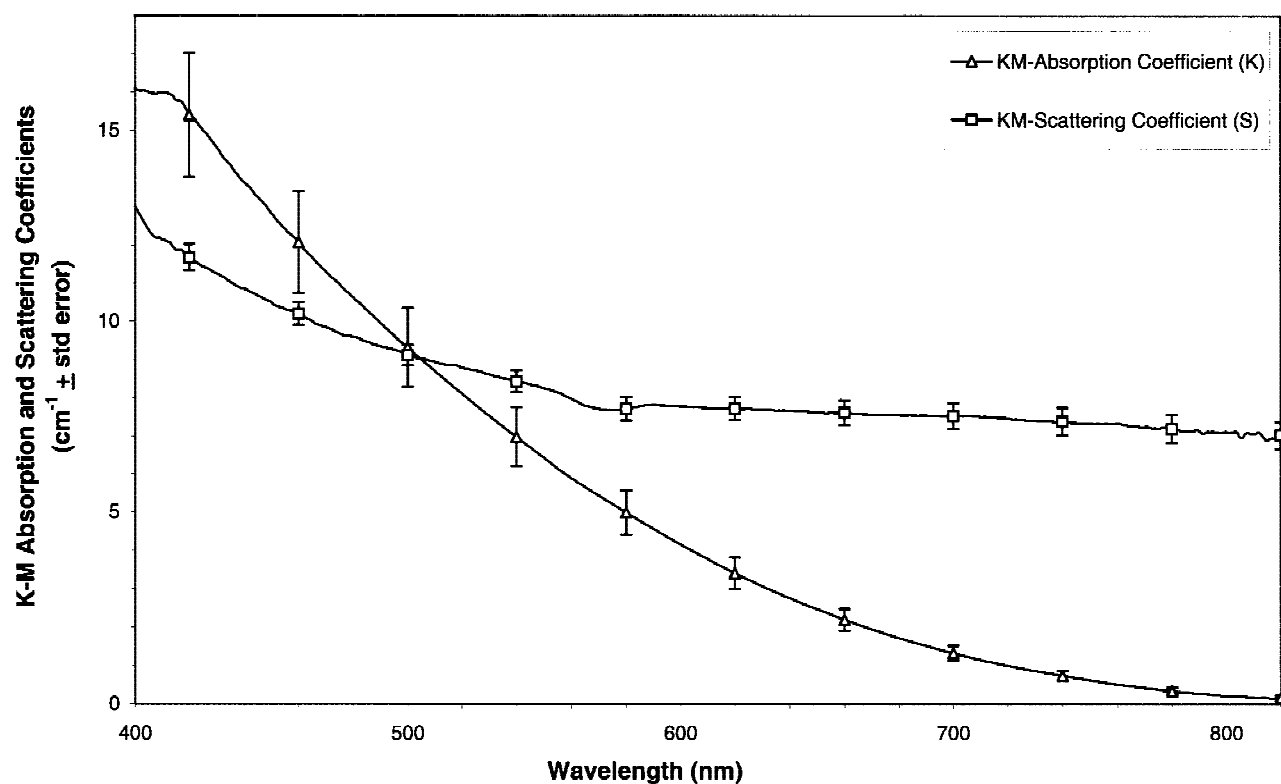


Fig. 4. Kubelka-Munk absorption (K) and scattering (S) coefficients. Data are plotted at wavelength intervals of 1 nm, while standard error bars are shown at wavelength intervals of 40 nm.

that is four times that of the argon treatment. This makes the fluence at the two wavelengths 4.07 kJ/cm<sup>2</sup> for the argon laser and 2.80 kJ/cm<sup>2</sup> for the diode laser. The energy attenuation plot, using these initial fluences, was plotted (Fig. 7). Note that while the fluence of the argon laser treatment is initially greater than that of the diode laser, deep in the TM, at or near Schlemm's canal, the fluence of the diode laser becomes higher than that of the argon laser, since attenuation at the argon wavelength is greater than at the diode wavelength. Comparing this crossover point of fluences between the estimated anisotropies of 0.85 and 0.90 reveals a shift of that point to shallower TM with increasing anisotropy (Fig. 7). Specifically, the crossover point shifts from 106  $\mu$ m at  $g = 0.85$  to 74  $\mu$ m at  $g = 0.90$ . This is meaningful because in relation to the thickness of TM, it indicates what regions of the TM receive a higher relative energy dose of one wavelength vs. another.

The fluence at any depth can be calculated by attenuating the initial fluence using  $\mu_t$  (Fig. 7). As previously stated, typical values of initial flu-

ence for the argon and diode laser are 4.07 kJ/cm<sup>2</sup> and 2.8 kJ/cm<sup>2</sup>, respectively. The total energy absorbed by the TM can then be calculated by calculating the fluence absorbed,  $dF$ , over thickness  $dx$ , at a given depth within the TM, and then summing these values over the entire TM thickness.

With the optical properties calculated in the current study, the fluence absorbed as a function of TM depth was plotted using numerical methods, for the estimated anisotropies of  $g = 0.85$  and 0.90 (Fig. 8). The total energy absorbed follows by summing the values of  $dF$  from  $x = 0$  to the TM full thickness, and then multiplying the sum by the area of the standard spot size used in argon (50  $\mu$ m) and diode (100  $\mu$ m) LT. Given the range of TM thickness, 90–130  $\mu$ m, the range of total energy absorbed in argon LT is 2.4–2.9 mJ for  $g = 0.85$ , and 2.0–2.3 mJ for  $g = 0.90$ . For diode LT, the total energy absorbed ranged from 0.133–0.172 mJ for  $g = 0.85$ , and 0.118–0.145 mJ for  $g = 0.90$ . Thus, there is approximately 17 times more energy absorbed in argon LT than diode LT.

One assumption made in standard Kubelka-Munk theory is that the propagating fluxes are

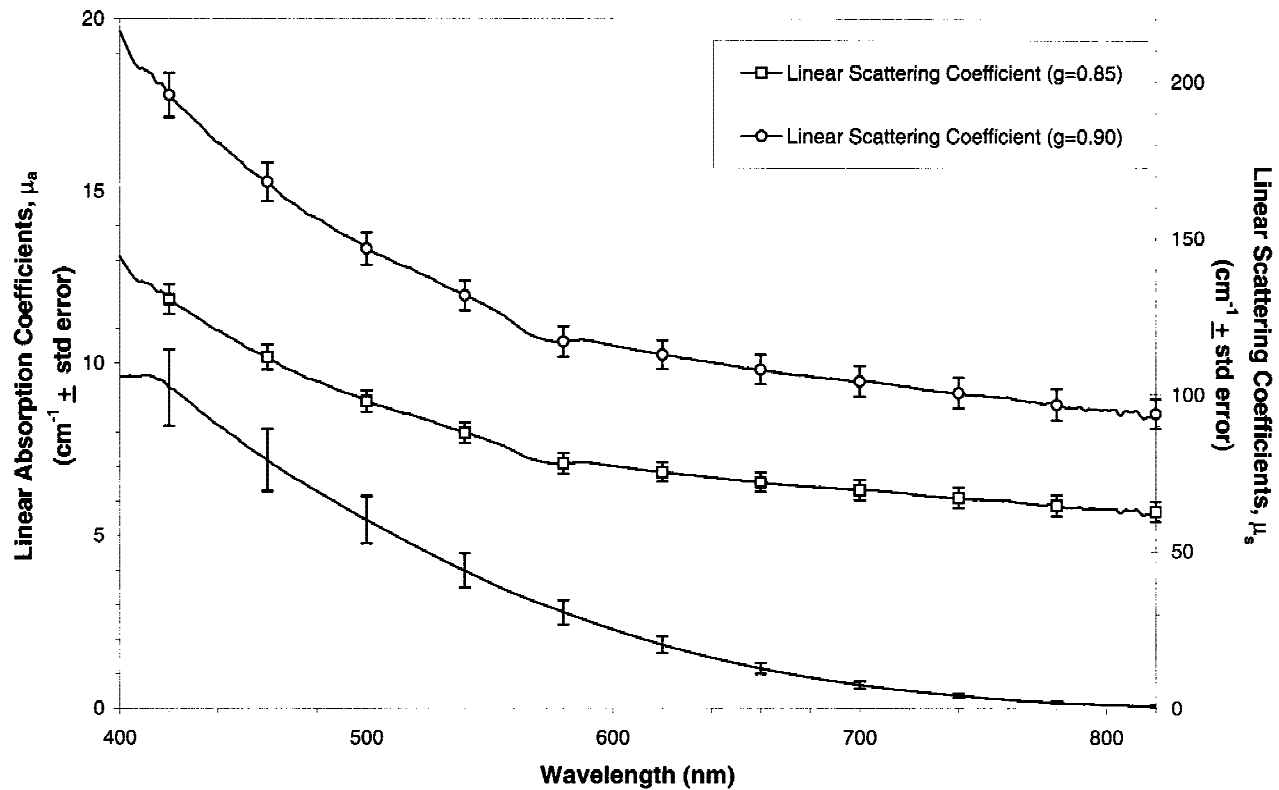


Fig. 5. TM linear transport absorption coefficient (left-axis scale) and scattering coefficient (right-axis scale) for estimated anisotropies  $g = 0.85$  and  $g = 0.90$ . Data are plotted at wavelength intervals of 1 nm, while standard error bars are shown at wavelength intervals of 40 nm.

TABLE 2. Optical Properties of TM, and Penetration Depths of Wavelengths Used Clinically in LT\*

	Argon laser (514.5 nm)		Diode laser (810 nm)	
	$g = 0.85$	$g = 0.90$	$g = 0.85$	$g = 0.90$
$\mu_a$ ( $\text{cm}^{-1} \pm \text{std dev}$ )	$4.89 \pm 1.95$	$4.89 \pm 1.95$	$0.0874 \pm 0.111$	$0.0874 \pm 0.111$
$\mu_s$ ( $\text{cm}^{-1} \pm \text{std dev}$ )	$94.13 \pm 10.53$	$141.20 \pm 15.80$	$62.96 \pm 10.02$	$94.44 \pm 15.03$
$\mu_t$ ( $\text{cm}^{-1} \pm \text{std dev}$ )	$99.021 \pm 12.49$	$146.09 \pm 17.03$	$63.051 \pm 10.12$	$94.53 \pm 15.14$
Penetration depth ( $1/e$ )	101 $\mu\text{m}$	69 $\mu\text{m}$	159 $\mu\text{m}$	106 $\mu\text{m}$
Penetration depth ( $1/e^2$ )	202 $\mu\text{m}$	139 $\mu\text{m}$	317 $\mu\text{m}$	212 $\mu\text{m}$

\*Std dev, standard deviation.

diffuse. Although the light incident on the sample is collimated, this light becomes quickly diffuse within in the sample and backing. Van Gemert et al. [43] stated that this effect is true if the sample thickness is much greater than the mean free scattering path length,  $\mu_s^{-1}$ . For TM,  $\mu_s^{-1}$  ranges from a minimum of 46  $\mu\text{m}$  ( $g = 0.9$ ) at 400 nm, to a maximum of 163  $\mu\text{m}$  ( $g = 0.85$ ) at 814.5 nm. This is approximately 4–13 times less than the sample thickness of 610  $\mu\text{m}$ . Thus, the fluxes can be considered diffuse.

TM from eight eyes was needed to provide for

each sample in spectral analysis, and each sample was homogenized to provide uniformity. Although it is known that scattering is dependent on material structure, to leave each sample unhomogenized would mean the results from the different heterogeneous samples would be incomparable. Vogel et al. [44] addressed similar issues in deriving KM optical properties of sclera for the wavelengths of 442, 514, 633, 804, and 1064 nm. Three sets of measurements were made, one with the fiber-optic light source separated from the sample, another with the fiber in “gentle” contact



## Relative Attenuation within TM

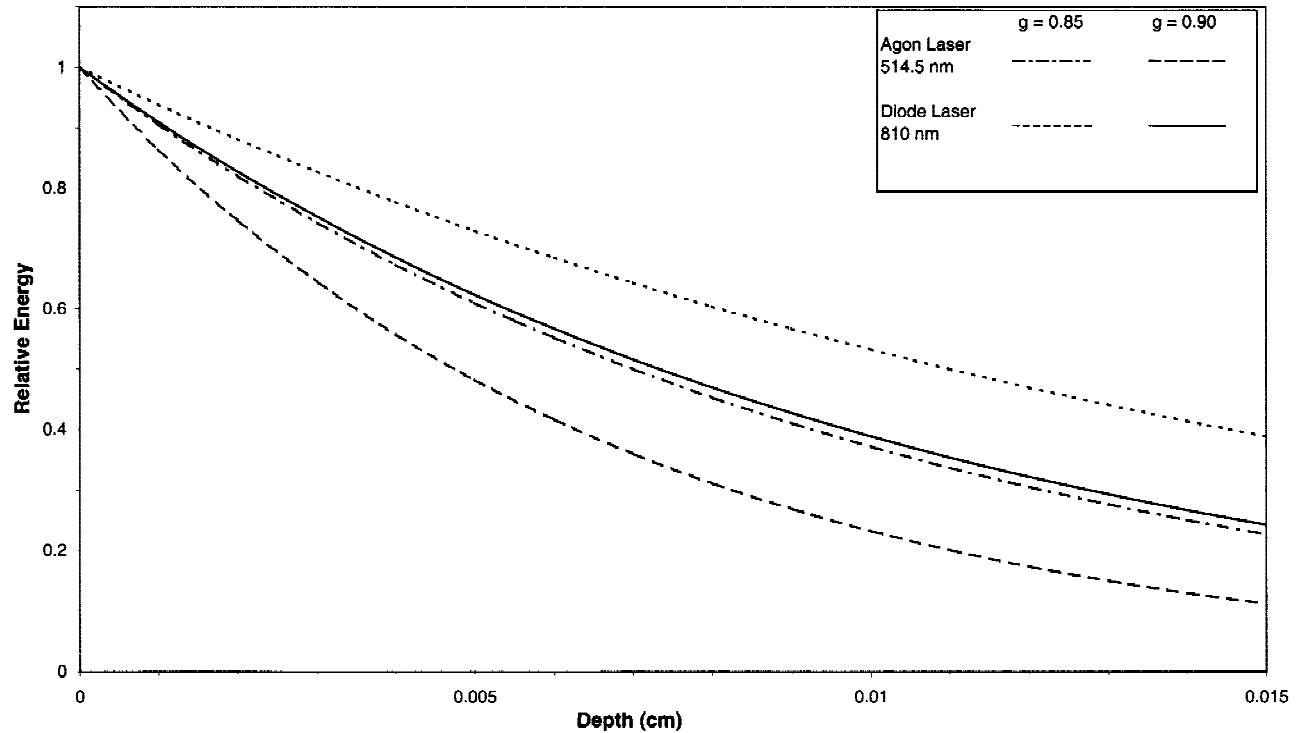


Fig. 6. Relative energy profile as a function of TM depth for estimated anisotropies  $g = 0.85$  and  $g = 0.90$ . Attenuation of the argon laser wavelength is greater than that of the diode laser wavelength. Higher anisotropy increases the scattering coefficient and thus the attenuation of laser energy.

with the sample, and the third with the fiber in “firm” contact with the sample. The value of  $S$  dropped with increased pressure, more at the lower than higher wavelengths. The explanation given for this phenomenon was an alteration of the physical makeup of the sclera, specifically a decrease in collagen fibril spacing. Therefore, the TM scattering may be greater in vivo than measured in the current study.

No attempt to characterize optical properties of TM was found in the literature. However, in the interest of verifying the current study, comparisons can be made to scleral optical properties, due to the similar constituents. In comparing the above authors’ KM optical properties of sclera to the TM properties in this study, the absorption coefficient,  $K$ , was of the same decreasing profile. Vogel et al. [44] reported that their  $K$  data for contact and noncontact measurements were the same. This supports the theory that  $S$  is dependent on structure, while  $K$  is dependent only on tissue constituents. After converting the data of Vogel et al. [44] to linear transport coefficients, the TM scattering coefficient in the current study fell between the sclera data for fiber contact with

both gentle pressure and firm pressure. This might mean that the scattering coefficients of TM in this study are lower than in the unhomogenized, in vivo state. However, due to the whiteness of the sclera, it would be normal to expect TM scattering to be somewhat less than scleral scattering.

Also reported by Vogel et al. [44], the absorption spectrum of sclera is similar to that of melanin. This is also true for TM, since its primary chromophore is also melanin. Vogel et al. [44] did not take into account interface reflection, nor they did they convert the KM coefficients to linear transport coefficients. In addition, in calculating their optical properties they did not measure the actual thickness of their samples, but used an average value reported in an ophthalmic reference.

Hammer et al. [33] also derived optical properties for sclera using porcine eyes, which they presented as a good human sclera model. Inverse Monte Carlo theory was used rather than KM theory, to calculate the linear transport absorption and scattering coefficient, as well as anisotropy. Because this theory is much more time-intensive than KM theory, Hammer et al. [33]

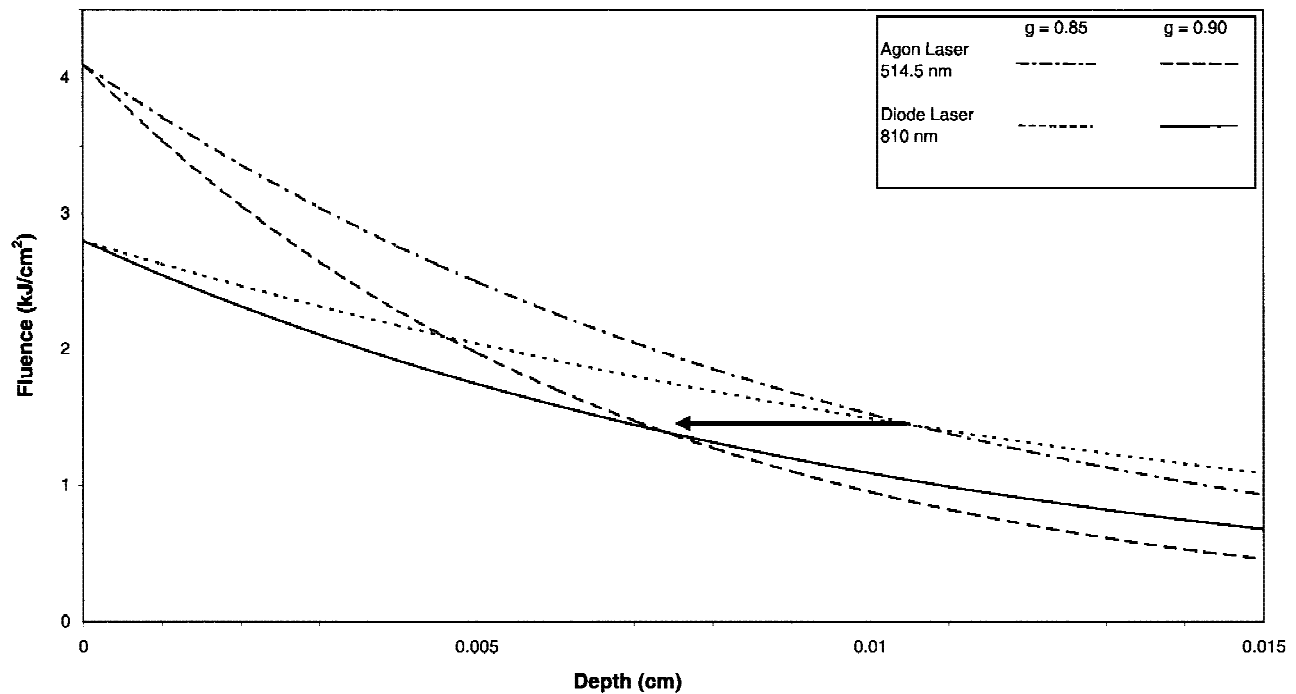


Fig. 7. Typical fluence profile as a function of TM depth for estimated anisotropies  $g = 0.85$  and  $g = 0.90$ . Argon LT fluence starts higher but falls below the diode LT fluence. Higher anisotropy shifts intersection (arrow) to shallower depths.

used 12 discrete wavelengths between 413–1,064 nm, as opposed to the 1-nm intervals used in the current study. An anisotropy of 0.9 was calculated at the wavelength of 1,064 nm and was assumed constant throughout the wavelengths of interest. The sclera samples were prepared by freezing and “mortarizing” the samples after using a cryoprotectant solution. The profiles of optical coefficients measured for sclera were very similar to that of TM. While the TM scattering coefficient declined from approximately  $144 \text{ cm}^{-1}$  to  $63 \text{ cm}^{-1}$  ( $g = 8.5$ , 400–820 nm), the sclera scattering coefficient declined from approximately  $1,470 \text{ cm}^{-1}$  to  $610 \text{ cm}^{-1}$  (413–780 nm). The TM and sclera absorption coefficient were of similar magnitude, with the former dropping from approximately  $9.62$  to  $0.081 \text{ cm}^{-1}$  (400–820 nm), and the latter from approximately  $7.1$  to  $0.40 \text{ cm}^{-1}$  (413–780 nm). As expected, the profile of the data from Hammer et al. [33] were similar to that of Vogel et al. [44], although the magnitudes were approximately twice as large. This could easily be the difference between human and porcine eyes, or because Vogel et al. [44] did not account for interface reflections and actual sample thickness. As evident from the white opaque tissue, the scatter-

ing coefficient of sclera is expected to be high. The difference in magnitude between the sclera and TM scattering coefficients is likely due to the density and orientation of collagen. These two factors are the reasons why the cornea, which has constituents similar to those of sclera but with a collagen fibril density 10 times that of sclera tissue [45], does not scatter light as scleral tissue does.

If therapeutic effects similar to those of argon LT are achieved with the deeper penetrating, less absorbed diode laser, then what is happening to the additional argon laser energy absorbed? One possible explanation supported by the current study is that the majority of argon laser energy deposited in the surface of the TM is causing permanent thermal damage that offsets the therapeutic effects. This thermal damage in turn is likely to further diminish the penetration of argon laser energy into deeper TM. The depth in Figure 7, after which the diode laser fluence is greater than the argon laser fluence, may be the depth critical to increased outflow. It has been proposed [3,25,46–49] that the main point of resistance in the outflow of aqueous humor occurs deep in the TM within the juxtacanalicular tissue. Since the diode laser causes less thermal damage

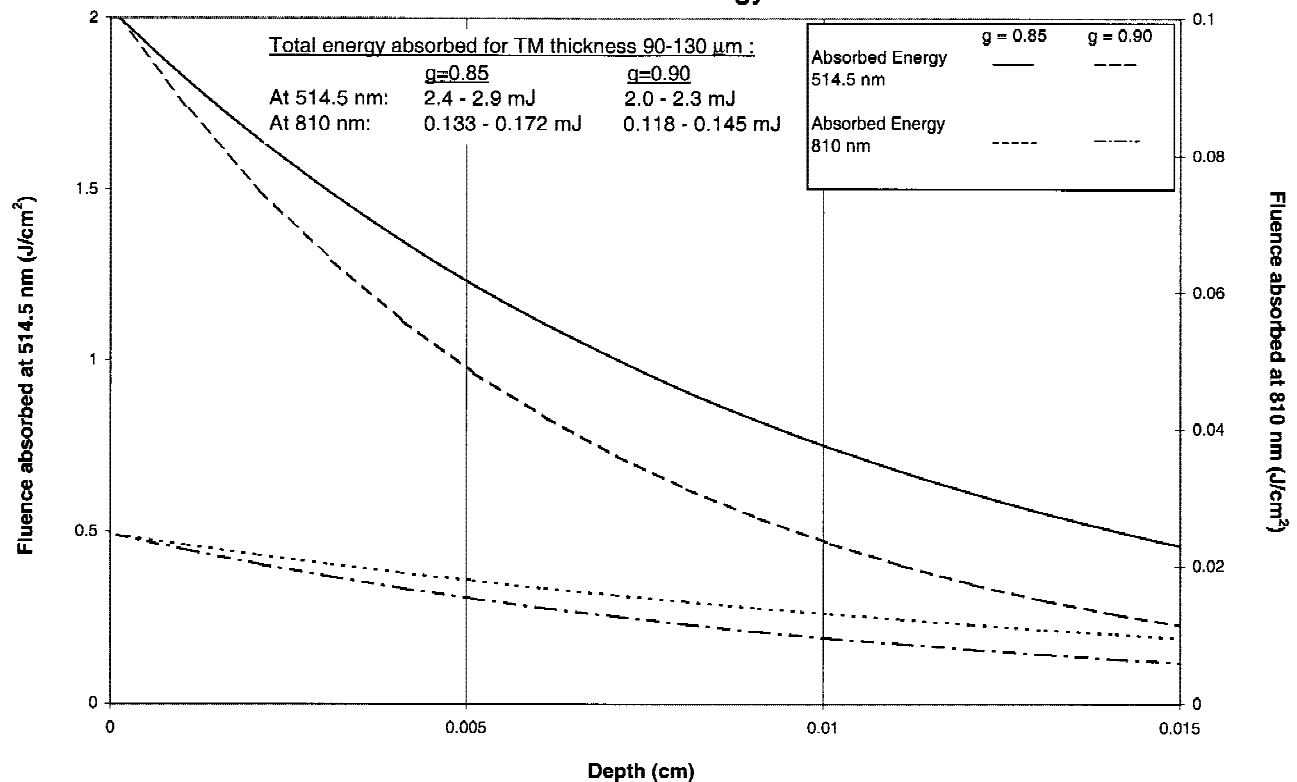


Fig. 8. Energy absorbed as a function of depth within TM. Values for 514.5 nm are plotted on the left axis, and values for 810 nm are plotted on the right axis. Total energy absorbed, given TM thickness of 90–130 nm and estimated anisotropies of  $g = 0.85$  and  $g = 0.90$ . Approximately 17 times more total energy is absorbed in diode LT vs. argon LT.

at the surface and is deeper penetrating than the argon laser, the two lasers may have similar therapeutic effects deep within the TM despite the differences in total energy deposited within the tissue. In fact, this could explain the mixed success of repeated argon LT, in that the thermal damage of argon LT may exceed the therapeutic effects upon retreatment. The results of repeated treatments of argon LT are inconsistent, ranging from unsuccessful to approximately 70% successful 1 year after retreatment [24,50]. The higher rates of success are usually seen in cases that previously showed at least 1 year of success following initial treatment of argon LT [50]. Unfortunately, the success or retreatment is short-term, with IOP controlled in 11–15% of cases at 2 years, and with IOP controlled in none at 5 years [50]. In contrast, there are no studies showing the success of repeat diode laser trabeculoplasty. It may be that retreatment with the diode laser would be more successful than with the argon laser, since less tissue damage occurs in diode laser treatment.

There have been studies that have at-

tempted to optimize LT by varying laser parameters. However, the parameter selections have been chosen mainly on a trial and error basis, without investigating the optical properties of the TM and attempting to predict optimal treatment parameters. Most of these studies showed success comparable to that of conventional argon laser trabeculoplasty [1,4,9]. After comparing the results of this study with quantified TM effects produced by lasers with carefully chosen parameters, efforts to optimize LT parameters may be more successful. The final goal is to make laser trabeculoplasty both successfully repeatable and a long-term solution to controlling a reduction in intraocular pressure.

A new procedure was recently introduced, called selective laser trabeculoplasty (SLT), which uses a Q-switched, frequency-doubled Nd:YAG laser emitting at 532 nm, close to the wavelength of the Argon ion laser [51,52]. Similar to argon LT, melanin is the target chromophore. Unlike argon LT, the energy is delivered in short pulses on the order of nanoseconds, which allows absorption to occur on a time scale much shorter than that of

thermal diffusion, thereby confining and limiting thermal effects. To model SLT, both the optical properties measured in the current study, as well as the thermal properties of the TM, would have to be taken into account. In early studies using the SLT energy delivery profile, trabeculoplasty was performed without the damage usually associated with visible wavelength irradiation of the TM [51], and yet successful lowering of IOP was achieved [52]. Interestingly, the maximum pulse energy used in a clinical procedure was 1.2 mJ per spot, much less than the total energy of a typical ALT spot using a similar wavelength. This provides further support for the argument that the therapeutic effect in LT actually requires less energy than previously thought, and the excess energy of the conventional ALT causes unnecessary thermal destruction. Despite this advance, the mechanism of action of LT remains elusive, and more work is needed to achieve the final goal of making laser trabeculoplasty both successfully repeatable and a long-term solution to controlling a reduction in intraocular pressure.

## APPENDIX: INTERFACE REFLECTIONS

### Section I: Single Boundary Mismatch

The scenario addressed by Saunderson [30] is near-collimated light incident on the boundary between air and a diffusely reflecting sample with a refractive index greater than air. This situation occurs often in spectral analysis. As shown in Figure 2, a fraction,  $k_1$ , of the incident light is reflected according to the Fresnel formula. The angles of the rays shown in Figure 2 are exaggerated to exhibit the reflection process. Of the light that is transmitted,  $(1 - k_1)$ , the fraction  $R$  is diffusely reflected and returns to the boundary. A fraction,  $k_2$ , of this diffuse light is reflected at the boundary back into the sample. The value of  $k_2$  is calculated using Walsh's theory [29], since diffuse light is traveling from a medium of a higher index of refraction to one of a lower index of refraction. This process continues, reflecting infinitely at the boundary. Upon each reflection at the boundary, the fraction of light that is not reflected is transmitted and can be written as the difference between unity and the reflection coefficient.

The desired measurement,  $R$ , is a property of the sample composition and structure. The reflectance measured by the spectrophotometer,  $R_M$ , can be written by summing the light exiting the sample (Fig. 2):

$$\begin{aligned} R_M &= k_1 + R(1 - k_1)(1 - k_2) + R^2 k_2(1 - k_1)(1 - k_2) \\ &\quad + R^3 k_2^2(1 - k_1)(1 - k_2) + R^3 k_2^2(1 - k_1)(1 - k_2) \\ &\quad + \dots = k_1 + R(1 - k_1)(1 - k_2) \sum_{i=0}^{\infty} [Rk_2]^i. \end{aligned} \quad (\text{Eq. 9})$$

Since reflection coefficients and their products are less than one, the following identity can be used for further simplification.

$$\sum_{i=0}^{\infty} b^i = \frac{1}{1 - b}, \quad \text{where} \quad b < 1. \quad (\text{Eq. 10})$$

This final version of  $R_M$  is thus obtained:

$$R_M = k_1 + \frac{R(1 - k_1)(1 - k_2)}{1 - Rk_2}. \quad (\text{Eq. 11})$$

Solving for  $R$  provides the necessary equation to extract the desired value of  $R$  from  $R_M$ :

$$R = \frac{R_M - k_1}{1 + k_2 R_M - k_1 - k_2}. \quad (\text{Eq. 12})$$

### Section II: Two-Boundary Mismatch

Deriving  $R$  from a more complicated scenario of two boundaries of mismatched refractive indices is a similar but more complex process than that addressed by Saunderson [30]. The first boundary in Figure 3 occurs between two nonattenuating mediums, layers 1 and 2. The second boundary is between the second and third layer, where the third layer is a diffuse reflecting sample. In this study, layer 1 is air ( $n_0 = 1$ ) and layer 2 is quartz glass ( $n_1 = 1.5$ ) that is covering the sample ( $n_2 = 1.37$ ). Light traveling from boundary 2 up towards boundary 1 is said to be traveling in the positive direction.

The layers involved are assumed to be optically linear materials, such that flux occurring within them can be added and subtracted in a linear fashion. The first step in solving for  $R$  is to represent the total spectral flux,  $F_1$ , traveling from boundary 1 toward boundary 2. This is shown in Figure 3 as the sum of light initially transmitted through boundary 1 and its reflections traveling in the negative direction. This infinite series can be represented similar to Equation 9 and simplified using the identity given in Equation 10:

$$\begin{aligned}
F_1 &= (1 - k_1) + (1 - k_1)k_1k_3 + (1 - k_1)k_1^2k_3^2 \\
&\quad + (1 - k_1)k_1^3k_3^3 + \dots \\
&= (1 - k_1) \sum_{i=0}^{\infty} [k_1k_3]^i = \frac{1 - k_1}{1 - k_1k_3}. \quad (\text{Eq. 13})
\end{aligned}$$

From spectral reflections, the values  $k_1$  and  $k_3$  are derived as Fresnel reflection coefficients. Because the critical angle for total internal reflection is irrelevant for light incident normal to a boundary, the spectral reflection coefficients at boundary 1 are the same for fluxes traveling in the positive and negative direction.

Of flux  $F_1$ , a fraction is reflected at boundary 2 and then transmitted through boundary 1. This is shown in Figure 3 and can be represented by

$$F_1k_3(1 - k_1). \quad (\text{Eq. 14})$$

Note that the portion of flux  $F_1$  reflected at boundary 2, traveling in the positive direction, is not reflected at boundary 1 because this reflection was already incorporated into  $F_1$ , as was shown in Figure 3.

The remainder of  $F_1$  is transmitted into layer 3 where it undergoes the same single boundary scenario observed by Saunderson [30], except that the reflection coefficient,  $k_4$ , represents the fraction of reflected diffuse light traveling from a lower to higher index of refraction rather than higher to lower. Thus,  $k_4$  is derived using the theory of Walsh [29], as represented in Equation 1. The diffuse light that reenters layer 2 in the positive direction can be represented as a single flux,  $F_2$ , using the same method as in the previous equation:

$$\begin{aligned}
F_2 &= F_1R(1 - k_3)(1 - k_4) + F_1k_4R^2(1 - k_3)(1 - k_4) \\
&\quad + F_1k_4^2R^3(1 - k_3)(1 - k_4) + F_1k_4^3R^4(1 - k_3) \\
&\quad (1 - k_4) + \dots = F_1R(1 - k_3)(1 - k_4) \sum_{i=0}^{\infty} [Rk_4]^i \\
&= \frac{F_1R(1 - k_3)(1 - k_4)}{1 - Rk_4}. \quad (\text{Eq. 15})
\end{aligned}$$

Flux  $F_3$  in Figure 3 represents the sum of  $F_2$  and all diffuse reflections immediately resulting from  $F_2$ , that are traveling in the positive direction:

$$\begin{aligned}
F_3 &= F_2 + F_2k_2k_5 + F_2k_2^2k_5^2 + F_2k_2^3k_5^3 + \dots \\
&= F_2 \sum_{i=0}^{\infty} [k_2k_5]^i = \frac{F_2}{1 - k_2k_5}, \quad (\text{Eq. 16})
\end{aligned}$$

where  $k_2$  and  $k_5$  are diffuse reflection coefficients for boundaries 1 and 2, respectively, for light traveling from a higher to lower index of refraction. They are derived using the theory of Richmond [28], as represented in Equation 2. The fraction of  $F_3$  that is transmitted through boundary 1 is

$$F_3(1 - k_2), \quad (\text{Eq. 17})$$

while the remainder is reflected at boundary 1 and reenters the sample.

All additional reflections and transmission are repeated steps of the processes explained above, starting by substituting  $F_3$  for  $F_1$ . As  $F_1$  produced  $F_2$  and  $F_3$ ,  $F_3$  produces  $F_4$  and  $F_5$ ,  $F_5$  produces  $F_6$  and  $F_7$ , etc. Below are the partially expanded equations of the fluxes,  $F_5$ ,  $F_7$ , and  $F_9$ , traveling in the positive direction.

$$F_5 = F_3 \left[ \frac{k_2R(1 - k_4)(1 - k_5)}{(1 - Rk_4)(1 - k_2k_5)} \right] \quad (\text{Eq. 18})$$

$$\begin{aligned}
F_7 &= F_5 \left[ \frac{k_2R(1 - k_4)(1 - k_5)}{(1 - Rk_4)(1 - k_2k_5)} \right] \\
&= F_3 \left[ \frac{k_2R(1 - k_4)(1 - k_5)}{(1 - Rk_4)(1 - k_2k_5)} \right]^2 \quad (\text{Eq. 19})
\end{aligned}$$

$$\begin{aligned}
F_9 &= F_7 \left[ \frac{k_2R(1 - k_4)(1 - k_5)}{(1 - Rk_4)(1 - k_2k_5)} \right] \\
&= F_3 \left[ \frac{k_2R(1 - k_4)(1 - k_5)}{(1 - Rk_4)(1 - k_2k_5)} \right]^3 \quad (\text{Eq. 20})
\end{aligned}$$

This pattern continues such that

$$F_{3+2N} = F_3P^N, \quad N = 0, 1, 2, 3, \dots, \quad (\text{Eq. 21})$$

where

$$P = \frac{k_2R(1 - k_4)(1 - k_5)}{(1 - Rk_4)(1 - k_2k_5)}.$$

The reflectance measured by the spectrophotometer,  $R$ , written in terms of the above fluxes and five reflection coefficients, is defined as the sum of



the fluxes that are transmitted from layer 2 into the layer 1, the air (Figure 3).

$$R_M = k_1 + F_1 k_3 (1 - k_1) + F_3 (1 - k_2) + F_5 (1 - k_2) + F_7 (1 - k_2) + \dots = k_1 + F_1 k_3 (1 - k_1) + (1 - k_2) \sum_{i=0}^{\infty} (F_{3+2i})^i. \quad (\text{Eq. 22})$$

Substituting equations 19, 21, 22, and 27 to expand the terms  $F_1$ ,  $F_3$ , and  $F_{3+2i}$  yields

$$R_M = k_1 + \frac{k_3(1 - k_1)^2}{1 - k_1 k_3} + \frac{R(1 - k_1)(1 - k_3)(1 - k_4)(1 - k_2)}{(1 - k_1 k_3)(1 - R k_4)(1 - k_2 k_5)} \sum_{i=0}^{\infty} P^i. \quad (\text{Eq. 23})$$

If  $P$  is less than one, then the identity in Equation 10 can be used to simplify Equation 23. The test for this was performed in a graphical manner. The values of  $k_1 - k_5$  were calculated based on the refractive indices of the three layers, and then  $P$  was plotted with respect to  $R$ . For this study, the value of  $P$  remained well below one for all realistic values of  $R$  ( $R < 1$ ). Thus the final equation for the measured reflectance is

$$R_M = k_1 + \frac{k_3(1 - k_1)^2}{1 - k_1 k_3} + \frac{R(1 - k_1)(1 - k_3)(1 - k_4)(1 - k_2)}{(1 - k_1 k_3)(1 - R k_4)(1 - k_2 k_5)} \left[ 1 - \frac{k_2 R (1 - k_4)(1 - k_5)}{(1 - R k_4)(1 - k_2 k_5)} \right]. \quad (\text{Eq. 24})$$

The analytical solution for  $R$  with respect to  $R_M$ , obtained using Mathcad software (Mathsoft, Inc., Cambridge, MA), is too long to be displayed here, but was coded in C to extract the values of  $R$  from  $R_M$ .

Although the indices of refraction in this study were such that  $n_0 < n_2 < n_1$ , Equation 24 is valid for refractive indices of other relationships. The proper reflection coefficients (Fresnel, Walsh, or Richmond) must be calculated for  $k_1 - k_5$ , and the condition that  $P < 1$  must be verified.

## ACKNOWLEDGMENTS

The authors thank Dr. Doug Johnson of the Mayo Clinic and Dr. Mark Johnson of MIT for their assistance validating TM anatomical dimen-

sions. Dr. Stuart Collins of Ohio State University provided assistance with optical theory and methods.

## REFERENCES

1. McHugh D, Marshall J, Ffytche T, Hamilton P, Raven A. Diode laser trabeculoplasty (DLT) for primary open-angle glaucoma and ocular hypertension. *Br J Ophthalmol* 1990;74:743-747.
2. Higginbotham E, Lee D, editors. Management of glaucoma: difficult glaucoma. Cambridge, MA: Blackwell Scientific Publications; 1994.
3. Richardson L. Argon laser trabeculoplasty: review. *J Am Optom Assoc* 1992;63:252-255.
4. Brancat R, Roberto C, Trabucchi G. Diode laser compared with argon laser for trabeculoplasty. *Am J Ophthalmol* 1991;112:50-55.
5. McMillan T, Stewart W, Legler U, Powers T, Nutaitis M, Apple D. Comparison of diode and argon laser trabeculoplasty in cadaver eyes. *Invest Ophthalmol Vis Sci* 1994;35:706-710.
6. Bishop K, Krupin T, Feitl M, Adelson A, Werner E. Bilateral argon laser trabeculoplasty in primary open-angle glaucoma. *Am J Ophthalmol* 1989;107:591-595.
7. Ritch R, Shields M, Krupin T. The glaucomas: glaucoma therapy, vol 3, 2nd ed. St. Louis: Mosby Year Book, Inc.; 1996. p 1575-1590.
8. McHugh D, Marshall J, Ffytche T, Hamilton P, Raven A. Ultrastructural changes of human trabecular meshwork after photocoagulation with a diode laser. *Invest Ophthalmol Vis Sci* 1992;33:2664-2671.
9. Moriarty A, McHugh J, Ffytche T, Hamilton P. Long-term follow-up of diode laser trabeculoplasty for primary open-angle glaucoma and ocular hypertension. *Ophthalmology* 1993;100:1614-1618.
10. Shields M. Textbook of glaucoma, 4th ed. Baltimore: Williams & Wilkins; 1998. p 475.
11. Ticho U, Neshner R. Laser trabeculoplasty in glaucoma: ten-year evaluation. *Arch Ophthalmol* 1989;107:844-846.
12. Lotti R, Traverso C, Murialdo U, Traverso C, Frau B, Calabria G. Argon laser trabeculoplasty: long-term results. *Ophthalmic Surg* 1995;26:127-129.
13. Elsás T, Johnsen H. Long-term efficacy of primary laser trabeculoplasty. *Br J Ophthalmol* 1991;75:34-37.
14. Moulin F, Le Mer Y, Haut J. Five-year results of the first 159 consecutive phakic chronic open-angle glaucomas treated by argon laser trabeculoplasty. *Ophthalmologica* 1991;202:3-9.
15. Eendebak G, Boen-Tan T, Bezemer P. Long-term follow-up of laser trabeculoplasty. *Doc Ophthalmol* 1990;75:203-215.
16. Shingleton B, Richter C, Dharma S, Tong L, Bellows A, Hutchinson B, Glynn R. Long-term efficacy of argon laser trabeculoplasty: a 10-year follow-up study. *Ophthalmology* 1993;100:1324-1329.
17. Ritch R, Liebmann J, Robin A, Pollack I, Harrison R, Levene R, Hagadus J. Argon laser trabeculoplasty in pigmentary glaucoma. *Ophthalmology* 1993;100:909-913.
18. Paul Y, Schuman J, Netland P, Lloyd-Muhammad R, Jacobs R. Five-year results of a randomized, prospective, clinical trial of diode vs. argon laser trabeculoplasty for

- open-angle glaucoma. *Am J Ophthalmol* 1998;126:185–190.
19. Wise J, Witter S. Argon laser therapy for open-angle glaucoma: a pilot study. *Arch Ophthalmol* 1979;97:319–322.
  20. Wise J. Glaucoma treatment by trabecular tightening with the argon laser. *Int Ophthalmol Clin* 1981;21:69–78.
  21. Thomas J, Simmons R. Laser trabeculoplasty: Results. In: Wilensky J, ed. *Laser therapy in glaucoma*. Norwalk, CT: Appleton-Century-Crofts; 1985. p 23–36.
  22. Weber P, Davidorf F, McDonald C. Scanning electron microscopy of argon laser trabeculoplasty. *Ophthalmic Forum* 1983;1:26–29.
  23. Van Der Zypen E, Fankhauser F, England C, Kwasniewska S. Morphology of the trabecular meshwork within monkey (*Macaca speciosa*) eyes after irradiation with the freerunning Nd:YAG laser. *Ophthalmology* 1987;94:171–179.
  24. Van Buskirk E. Pathophysiology of laser trabeculoplasty. *Surv Ophthalmol* 1989;33:264–272.
  25. Acott T. What causes glaucoma and why does laser trabeculoplasty ameliorate it? Testing a hypothesis. 12th National Eye Research Seminar by Research to Prevent Blindness; 1993. p 20–22.
  26. Bylsma S, Samples J, Acott T, Van Buskirk E. Trabecular cell division after argon laser trabeculoplasty. *Arch Ophthalmol* 1988;106:544–547.
  27. Johnston W, O'Brien W, Tien T. The determination of optical absorption and scattering in translucent porcelain. *Color Res Appl* 1986;11:125–130.
  28. Richmond J. Relation of emittance to other optical properties. *J Res Natl Bur Standards [C]* 1963;67:217–226.
  29. Walsh JWT. The reflection factor of a polished glass surface for diffused light. Appendix to: Billmeyer FW, Alman DH. Exact calculation of Fresnel reflection coefficients for diffuse light. *J Color Appearance* 1973;II(1):36–38.
  30. Saunderson J. Calculation of the color of pigmented plastics. *J Optic Soc Am* 1942;32:727–736.
  31. Maurice DM. The cornea and sclera In: Davson H, editor. *The eye*, vol I. New York: Academic Press; 1962. p 289–368.
  32. Fine I, Loewinger E. Optical properties of sclera. *Phys Med Biol* 1985;30:565–571.
  33. Hammer M, Roggan A, Schweitzer D, Müller G. Optical properties of ocular fundus tissues—an in vitro study using the double-integrating-sphere technique and inversion Monte Carlo simulation. *Phys Med Biol* 1995;40:963–978.
  34. Enoch J, Tobey F Jr. Use of the waveguide parameter V to determine difference in the index of refraction between the rat rod outer segment and the interstitial matrix. *J Optic Soc Am* 1978;68:1130–1134.
  35. Mandell R. Corneal power correction factor for photorefractive keratectomy. *J Refract Corn Surg* 1994;10:125–128.
  36. Kubelka P. New contributions to the optics of intensely light-scattering materials. Part I. *J Optic Soc Am* 1947;38:448–457.
  37. van Gemert M, Star W. Relations between the Kubelka-Munk and the transport equation models for anisotropic scattering. *Lasers Life Sci* 1987;1:287–298.
  38. Cheong W, Prahl S, Welch A. A review of the optical properties of biological tissues. *IEEE J Quantum Electronics* 1990;26:2166–2185.
  39. Cheong W. Appendix to Chapter 8: Summary of optical properties. In: Welch A, van Gemert M, eds. *Optical-thermal response of laser-irradiated tissue*. New York: Plenum Press; 1995. p 275–303.
  40. Duane TD, Jaeger EA. In: *Biomedical foundations of ophthalmology*, vol I. Philadelphia: Harper & Row Publishers; 1986.
  41. McMenamin P, Lee W, Aitken D. Age-related changes in the human outflow apparatus. *Ophthalmology* 1986;93:194–209.
  42. Hogan M, Alvarado J, Weddell J. The limbus. In: *Histology of the human eye*. Philadelphia: W.B. Saunders Co.; 1971. p 112–182.
  43. van Gemert M, Welch A, Star W, Motabedi M, Cheong W. Tissue optics for a slab geometry in the diffusion approximation. *Lasers Med Sci* 1987;2:295–305.
  44. Vogel A, Dlugos C, Nuffer R, Birngruber R. Optical properties of human sclera, and their consequences for transscleral laser applications. *Lasers Surg Med* 1991;11:331–340.
  45. Borchering M, Blacik L, Sittig R, Bizzell J, Breen M. Proteoglycans and collagen fiber organization in human corneosclera tissue. *Exp Eye Res* 1975;21:59–70.
  46. Seiler T, Kriegerowski M, Pamer A, et al. Partial external trabeculectomy with the excimer laser: an experimental investigation of a new treatment for glaucoma. *Laser Light Ophthalmol* 1990;3:97–109.
  47. Parshley D, Bradley J, Fisk A, Samples J, van Buskirk E, Acott T. Laser trabeculoplasty induces stromelysin expression by trabecular juxtacanalicular cells. *Invest Ophthalmol Vis Sci* 1996;37:795–804.
  48. Francios J. The importance of the mucopolysaccharides in intraocular pressure regulation. *Invest Ophthalmol* 1975;14:173–176.
  49. Ethier C, Kamm R, Palaszewski B, Johnson M, Richardson T. Calculations of flow resistance in the juxtacanalicular meshwork. *Invest Ophthalmol Vis Sci* 1986;27:1741–1750.
  50. Feldman R, Katz L, Spaeth G, Crapotta J, Fahmy I, Moones A. Long-term efficacy of repeat argon laser trabeculoplasty. *Ophthalmology* 1991;98:1061–1065.
  51. Latina M, Park C. Selective targeting of trabecular meshwork cells: in vitro studies at pulsed and CW laser interactions. *Exp Eye Res* 1995;60:359–371.
  52. Latina M, Sibayan S, Shin DH, Noecker RJ, Marcellino G. Q-switched 532-nm Nd:YAG laser trabeculoplasty (selective laser trabeculoplasty), a multicenter, pilot, clinical study. *Ophthalmology* 1998;105:2082–2090.